

Development of an Enhanced Electromagnetic Actuation System With Enlarged Workspace

Fuzhou Niu, Junyang Li, Weicheng Ma, Jie Yang, and Dong Sun¹, Fellow, IEEE

Abstract—Electromagnetic actuation is an emerging wireless control approach for manipulating magnetic microparticles for diverse minimally invasive therapy and diagnosis. This paper presents an enhanced electromagnetic manipulation system with an enlarged workspace, which is achieved by both the parametric design and the quantitative modeling of generated magnetic field of the system. The parametric design aims to characterize the influence of electromagnet parameters, such as position, radius, and height of cores on the generated electromagnetic field, so that the electromagnet specifications of the developed system can achieve a large workspace, while possessing the desired magnetic field flux density (MFFD) and gradient. With this design, the workspace of the developed prototype can reach a spherical volume with a diameter of 110 mm, the MFFD can reach 100 mT, and the gradient of MFFD can reach 2.5 T/m. The spatial distribution of electromagnetic field is quantitatively modeled using the finite-element method. Based on this model, a unit electromagnetic field distribution database for a 3-D grid of points is established. Such database enables the effective manipulation of microparticles in a considerably large workspace rather than only small central area. Experiments of manipulating paramagnetic microparticles in both 2-D and 3-D scenarios are performed to demonstrate the effectiveness of the designed system.

Index Terms—Electromagnetic actuation, magnetic field distribution, magnetic microparticles.

I. INTRODUCTION

REMOTE manipulation of microparticles has attracted considerable attention in recent years, for its great potential in

Manuscript received December 18, 2016; revised May 8, 2017; accepted July 13, 2017. Date of publication August 21, 2017; date of current version October 13, 2017. Recommended by Technical Editor W. Li. This work was supported in part by the Research Grants Council of the Hong Kong Special Administrative Region, China, under Grant CityU 11267916. (Corresponding author: Dong Sun.)

F. Niu is with the Department of Precision Machinery and Instrumentation, University of Science and Technology of China, Hefei 215123, China, and also with the Department of Mechanical and Biomedical Engineering, City University of Hong Kong, Kowloon, Hong Kong (e-mail: fznui1988@163.com.).

J. Li, W. Ma, and D. Sun are with the Department of Mechanical and Biomedical Engineering, City University of Hong Kong, Kowloon, Hong Kong (e-mail: junyangli3-c@my.cityu.edu.hk; mweicheng2@cityu.edu.hk; medsun@cityu.edu.hk).

J. Yang is with the Department of Precision Machinery and Instrumentation, University of Science and Technology of China, Hefei 215123, China (e-mail: jieyang@ustc.edu.cn).

Color versions of one or more of the figures in this paper are available online at <http://ieeexplore.ieee.org>.

Digital Object Identifier 10.1109/TMECH.2017.2743021

the *in vivo* applications for biomarking, biosensing, bioscaffolding, and biomedicine. One of the most promising applications is the remote-controllable targeted delivery of biomaterials for minimally invasive surgery [1]–[4].

The manipulation of microparticles fundamentally depends on actuation systems. Researchers have proposed several actuation strategies for propelling microparticles based on diverse propulsion principles, covering multiple areas of biology, thermology, chemistry, optics, dielectrophoresis, microfluidics, electrostatics, and electromagnetic engineering [5]–[8]. Using magnetic fields to actuate microparticles have been explored because electromagnetic actuation can be a safe and wireless method to manipulate magnetic microparticles *in vivo* [9]. Benefitting from noncontact manipulation and flexibility in a confined environment, magnetic-driven microparticles can navigate into an *in vivo* environment for diverse minimally invasive therapeutic and diagnostic applications [10]–[13]. To date, an increasing number of magnetic actuated manipulation systems have been developed recently.

Three methods have been commonly used for designing and constructing a magnetic manipulation system, using permanent magnets, Helmholtz and/or Maxwell coils, and electromagnetic coils [14]–[18]. A permanent magnet can generate large magnetic field flux density (MFFD) and gradient efficiently and economically [19], but the generated field cannot be switched off easily because of residual magnetism; also, the change of the generated magnetic field is commonly realized by mechanical methods. Helmholtz and Maxwell coils can produce a magnetic field with uniform magnetic field density and gradient, bringing convenience to both modeling and control. However, the generated magnetic field usually possesses weak strength and small workspace. Compared to the above two methods, the method with electromagnetic field exhibits the advantage of providing a remote-controllable source for untethered agents with high magnetic characteristics in a relatively large workspace. Various electromagnetic systems have been reported in the literature [20]–[26], with different characters of electromagnet configuration, workspace, and magnetic field distributions. An electromagnetic system called Octomag [17] was designed aiming at delicate retinal procedures, providing a semispherical workspace of 130 mm diameter. An electromagnetic system composed of five independent electromagnetic coils, called Mag- μ Bot system, was proposed in [27], providing a workspace with a cubic volume of $100 \times 100 \times 100 \text{ mm}^3$. An electromagnetic system that contained eight air-core electromagnets was designed in [28], providing a workspace of

120 × 120 × 120 mm³ cube. A magnetic actuation system with a 2-D workspace of 2.4 × 1.8 mm², focusing on manipulating microparticles in the vertical direction, was designed in [29]. All these developed systems suffered from a limitation that the microparticles can be manipulated effectively only at the central area of the workspace. These systems cannot be used for *in vivo* study on animals, such as mouse and rabbit, due to the small workspace. *In vivo* study of manipulating microagents inside animals plays an increased important role in biomedical research today. Currently, few magnetic manipulation devices can provide an effective workspace that is large enough for doing real-time animal tests.

This paper reports our new development of an enhanced electromagnetic actuation system utilizing electromagnetic coils, which can generate a large workspace. It must be emphasized that providing a large workspace while maintaining high electromagnetic filed flux density and gradient is a challenging problem, which cannot be solved by simply using large coil dimensions. In fact, as the gap between electromagnets increases, the workspace increases, but meanwhile, the MFFD and gradient decrease. Simply increasing the supply power of coils is not the ideal way to solve the problem because the coil power supply is subject to the constraints of the current limitation and the heating generation. To achieve a large workspace while possessing high magnetic strength, we need to take many factors, such as energy supply, manufacture cost, saturation of magnetic cores, space amongst coils (to avoid potential collisions), space left for imaging process, and other manual operations, etc., into account. Besides the system hardware design, we also need to design an effective manipulation strategy, which requires the quantitative modeling information for precise spatial distribution of the electromagnetic field. All these factors motivated the current research.

We have performed this research in the following two perspectives.

First, we characterized the influence of electromagnet parameters, such as position, radius, and height of cores on the generated electromagnetic field. Based on the characterization, we designed the electromagnet specifications of the developed system that could achieve a large workspace while possessing the desired MFFD and gradient. The workspace of the designed system was enlarged to a spherical volume with a diameter of 110 mm. The generated MFFD could reach 100 mT, and the gradient of the MMFD could reach 2.5 T/m. This new manipulation system is advantageous both in the size of workspace and strength of generated magnetic field.

Second, we modeled quantitatively the spatial distribution of the electromagnetic field using the finite-element method (FEM), and verified the validity of this model through comparison between modeling and experimental results. Based on this model, we further established a unit electromagnetic field distribution database for a 3-D grid of points, and calculated the generated magnetic field at these specified points. The information of the magnetic field at the other points of the workspace was obtained by using trilinear interpolation. With this modeling information, we could successfully manipulate the microparticles effectively in a larger workspace than the central area only. Ex-

periments of tracking microparticles with Fe₃O₄ nanoparticles in both 2-D and 3-D scenarios have been performed successfully in the enlarged workspace to demonstrate the effectiveness of the designed system.

Our developed system is relevant to several existing systems, such as Octomag system [17], Mag-μBot system [27], and the system in [28], but features major differences. In the Octomag system [17], all the eight electromagnets are installed above the workspace. This design provides the benefit of viewing the controlled particles by installing a microscope below the workspace, but has difficulty to generate downward magnetic forces. In our system, all the six electromagnets are installed surrounding the workspace to produce 3-D magnetic forces in both downward and upward directions, thus providing the advantage of the vertical controllability of the controlled particles. In the system [28], all the electromagnets are also installed surrounding the workspace, but with smaller magnetic flux density and gradient to be generated. In all the systems of [17], [27], and [28], the microparticles are manipulated effectively only at the central area of the workspace. In our system, the microparticles can be manipulated effectively in a much larger region. Table I illustrates a comparison between our developed system and several existing electromagnetic coils actuation systems.

II. SYSTEM DESIGN

A. Magnetic Force and Torque

A microparticle, when located in a magnetic field, is subject to a force \mathbf{F} contributing to particle translation (or translational trend) and a torque \mathbf{T} resulting in particle rotation (or rotational trend). Both force and torque rely on the magnetic nature of the particle and the distribution of the magnetic field. The mathematical expressions of the force and torque acting on the particle, with magnetic moment \mathbf{m} under a magnetic field \mathbf{B} , can be written as

$$\mathbf{F} = (\mathbf{m} \cdot \nabla) \mathbf{B} = \begin{bmatrix} \frac{\partial B_x}{\partial x} & \frac{\partial B_x}{\partial y} & \frac{\partial B_x}{\partial z} \\ \frac{\partial B_y}{\partial x} & \frac{\partial B_y}{\partial y} & \frac{\partial B_y}{\partial z} \\ \frac{\partial B_z}{\partial x} & \frac{\partial B_z}{\partial y} & \frac{\partial B_z}{\partial z} \end{bmatrix} \mathbf{m} \quad (1)$$

$$\mathbf{T} = \mathbf{m} \times \mathbf{B} = \begin{bmatrix} e_x & e_y & e_z \\ m_x & m_y & m_z \\ B_x & B_y & B_z \end{bmatrix} \quad (2)$$

where x, y, z are three coordinates in the Cartesian space, $\mathbf{B} = (B_x, B_y, B_z)^T$, $\mathbf{m} = (m_x, m_y, m_z)^T$, $(e_x, e_y, e_z)^T$ donates the identity matrix, and ∇ is a gradient operator.

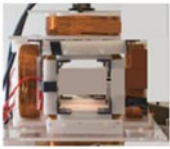



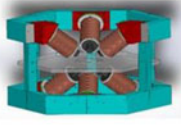
Given that the workspace of the magnetic manipulation system is a current-free space, the quasi-static magnetic field is considered. We derive the following expressions based on Maxwell's equations:

$$\nabla \cdot \mathbf{B} = 0 \quad (3)$$

$$\nabla \times \mathbf{B} = \mu_0 \mathbf{J} \quad (4)$$

where \mathbf{J} is the current density and μ_0 represents the magnetic permeability in a classical vacuum. We then obtain the following

TABLE I
COMPARISON OF SEVERAL EXISTING ELECTROMAGNETIC COILS SYSTEMS AND OUR SYSTEM

System [reference]	Mag-uBot [27]	Octomag [17]	System A [28]	System B [29]	Our system
Electromagnet Configuration					
Electromagnet number	6	8	8	4	6
Core material	Air	VACOFLUX 50	Air & Iron	Air	DT4E
Current intensity (A)	3	15	19	Unknown	10
Physical space	100mmx100mmx100mm	Semisphere diameter:130mm	120mmx120mmx120mm	40mmx40mm	Sphere diameter:110mm
Center area of workspace	20mmx20mmx20mm	Semisphere diameter:25mm	20mmx20mmx20mm	24mmx18mm	sphere diameter:~20mm
Maximum field flux at center	6.5mT	15mT	15mT	15mT	~40mT
Maximum gradient at center	149mT/m	~200mT/m	~100mT/m	60mT/m	~250mT/m
Microagent material	NdFeB	Ni/CoNi	NdFeB/Iron	Paramagnetic	Paramagnetic
Effective manipulation space	Center of workspace	Center of workspace	Center of workspace	Center of workspace	Almost whole workspace

expressions:

$$\sum_{\alpha}^{x,y,z} \frac{\partial B_{\alpha}}{\partial \alpha} = 0 \quad (5)$$

$$\frac{\partial B_{\alpha}}{\partial \beta} = \frac{\partial B_{\beta}}{\partial \alpha} \quad (\alpha, \beta = x, y, z). \quad (6)$$

By substituting (5) and (6) into (1), the force can be written as follows:

$$\mathbf{F} = \begin{bmatrix} \frac{\partial B_x}{\partial x} & \frac{\partial B_x}{\partial y} & \frac{\partial B_x}{\partial z} \\ \frac{\partial B_y}{\partial x} & \frac{\partial B_y}{\partial y} & \frac{\partial B_y}{\partial z} \\ \frac{\partial B_z}{\partial x} & \frac{\partial B_z}{\partial y} & -\left(\frac{\partial B_x}{\partial x} + \frac{\partial B_y}{\partial y}\right) \end{bmatrix} \mathbf{m}. \quad (7)$$

Equation (2) can be rearranged as

$$\mathbf{T} = \begin{bmatrix} 0 & B_z & -B_y \\ -B_z & 0 & B_x \\ B_y & B_x & 0 \end{bmatrix} \mathbf{m}. \quad (8)$$

As shown in (7) and (8), the magnetic force and the torque acting on a particle are functions of the distribution of the applied external magnetic field and its gradient. Thus, calculating the field distribution of a magnetic manipulation system is crucial; it forms a basis for actuating magnetic microparticle in magnetic fields.

B. Parametric Analysis for Electromagnetic Coils Design

Inspired by the Descartes coordinates, a common orthogonal configuration of six electromagnets pointing at a common center was chosen in the design. Skew configuration was utilized in order to provide a suitable space for installing a microscope while avoiding potential collisions.

Parameters of position, radius, and height of cores, as shown in Fig. 1(a), all correspond to electromagnet configuration. These parameters were analyzed first using the FEM. The analysis was based on two electromagnets, where the upper coil was conducted with 1-A clockwise current while the lower coil was not powered. The parametric design process was performed automatically using the “optimetric analysis” function in Ansys

electronics desktop suite, during which the values of parameters were calculated in linear step. Besides these three parameters, some other parameters, such as the geometry of the core and the distribution of turns of coils, also have influence on the generated magnetic field. Since the three parameters of position, heights, and radius of cores affect more significantly to the electromagnet configuration than others, we mainly analyzed these three parameters in this research. The parametric design aimed to characterize the influence of the position, radius, and height of cores on the generated electromagnetic field. Based on this analysis, the parameters used for the prototype system were finally determined.

The influence of core position (termed “core_position” here) on the MFFD \mathbf{B} was initially analyzed, as shown in Fig. 1(b). Table II lists the parameters used for the core_position analysis. In the numerical analysis, the minimum of core_position was set as 45 mm to leave a space for installing a microscope, and stranded-type current was used to obtain a uniform current density throughout the conductor. Results in Fig. 1(b) clearly indicate that the magnitude of MFFD decreases as the value of core_position increases. A large value of core_position results in a large gap, and, thus, a large volume of workspace, but it also decreases the value of MFFD. Balance must be considered in determining the value of the core_position.

The influence of the core height (termed “core_height” here) on the MFFD \mathbf{B} was second analyzed, as seen in Fig. 1(c). Table III introduces the parameters used for the core_height analysis. Stranded-type current was also used in this analysis. Results in Fig. 1(c) show that the variation of core_height causes almost no change to the MFFD, which can be explained as follows. The electromagnet configuration was designed based on many factors including characteristics of the generated magnetic field, positions of coils, the gap between two oppositely placed coils in the workspace, space used for manual work and imaging process, etc. All these factors resulted in the use of long-size electromagnets in our system. With long-size electromagnet, the increase of core_height produced relatively little effect to the generated field. In our prototype, we chose a core_height of 275 mm that corresponded to 1720 turns of enameled wire around the core.

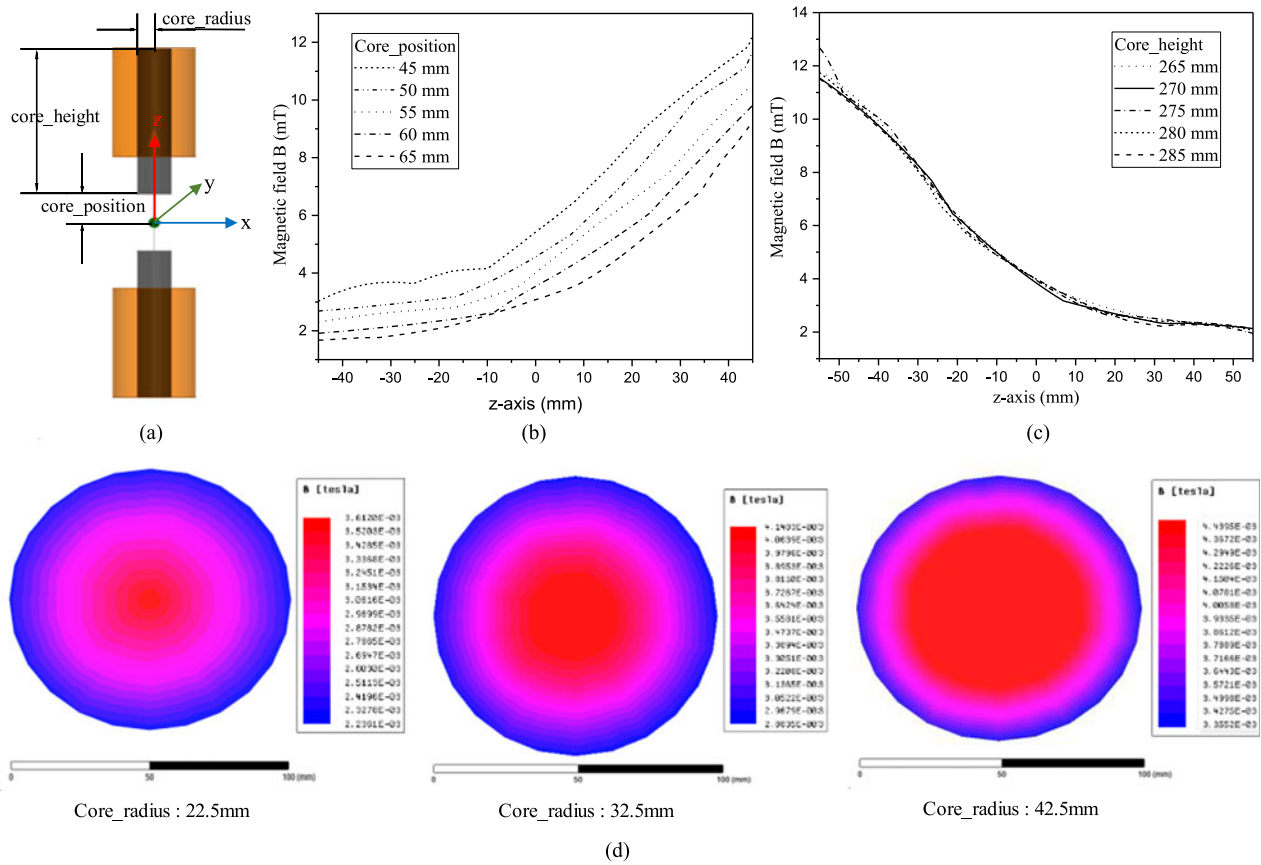


Fig. 1. (a) Parametric-analyzing model based on two electromagnets. The upper coil is conducted with 1-A clockwise current, while the lower coil is not powered. (b) Numerical results of the MFFD varied along z-axis at different positions of core. (c) Numerical results of the MFFD varied along z-axis with different heights of core. (d) Numerical results of the MFFD at $z = 0$ in a 100-mm-diameter circle, with different radii of core of 22.5, 32.5, and 42.5 mm.

TABLE II
PARAMETERS USED FOR CORE_POSITION ANALYSIS

Coil	outer radius	77.5 mm
	inner radius	32.5 mm
	position at z-axis	core_position + 70 mm
	coil height	205 mm
Core	radius	32.5 mm
	position at z-axis	parametric designed
	core height	275 mm
Conducting Current	number of coil turns	1720
	current	1 A
	current type	stranded

TABLE III
PARAMETERS USED FOR CORE_HEIGHT ANALYSIS

Coil	outer radius	77.5 mm
	inner radius	32.5 mm
	position at z-axis	125 mm
	coil height	Core_height—70 mm
Core	radius	32.5 mm
	position at z-axis	55 mm
	core height	parametric designed
Conducting Current	number of coil turns	1720
	current	1 A
	current type	stranded

TABLE IV
PARAMETERS USED FOR CORE_RADIUS ANALYSIS

Coil	outer radius	core_radius + 45 mm
	inner radius	core_radius
	position at z-axis	125 mm
	coil height	205 mm
Core	radius	parametric designed
	position at z-axis	55 mm
	core height	275
Conducting Current	number of coil turns	1720
	current	1 A
	current type	stranded

Finally, the influence of the core radius (termed “core_radius” here) on the MFFD B was analyzed, as shown in Fig. 1(d). Table IV presents the parameters used for the core_radius analysis. In the analysis, the MFFD was calculated at a position of $z = 0$ in a circular area with a diameter of 100 mm, and stranded-type current was used as well. The results in Fig. 1(d) demonstrate that as the core_radius increases, the area of uniform magnetic field enlarges, which benefits a large controllable workspace. In our design, we chose a core_radius of 37.5 mm to balance workspace area and core mass.

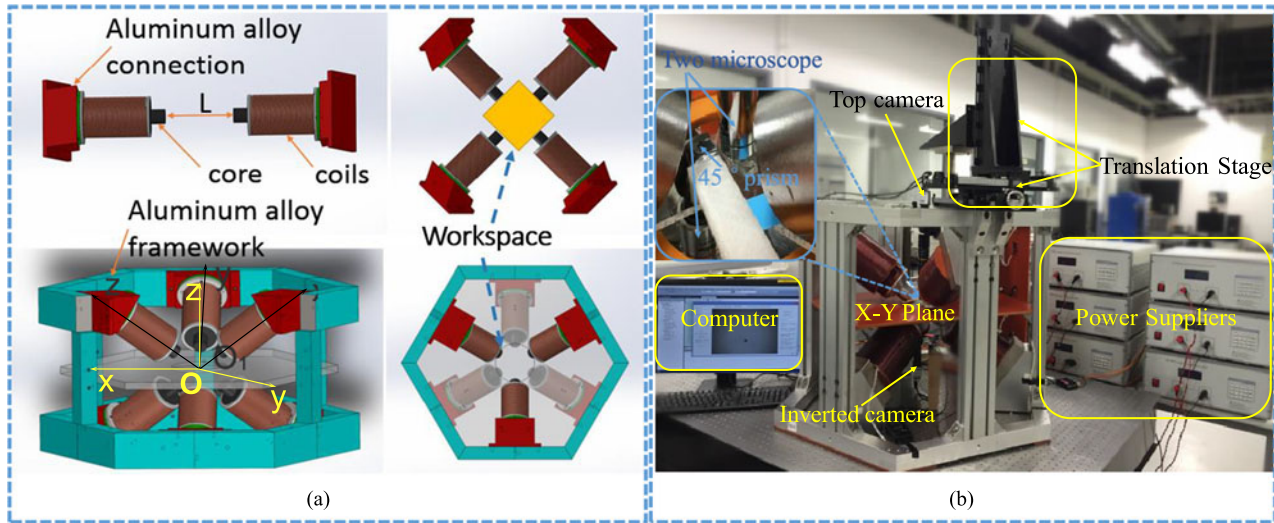


Fig. 2. Home-designed electromagnetic manipulation system. (a) Schematic. (b) System setup.

TABLE V
PARAMETERS OF EACH ELECTROMAGNETIC COIL

Description	Value	Units
Material of coils	enameled copper wire	
Coil resistance (R)	3.2	Ω
Inner diameter of coils	65	mm
Outer diameter of coils	155	mm
No. of wire turns	~ 1720	
Distance from center ($L/2$)	55	mm
Material of cores	DT4E	
Diameter of core	65	mm
Length of core	275	mm
Volume of workspace	$110 \times 110 \times 110$	mm^3

Based on the analysis from these three perspectives, the parameters used for our machine prototype design were finally determined (see Table V). The generated magnetic field B depends on the value of input current I as well as the specifications of coils, such as coil arrangement, coil turn number, core material, and core geometry. Provided that these specifications of an electromagnetic system are determined, the magnetic field distribution will largely depend on the input current.

C. Magnetic Manipulation System

Based on the parameters of electromagnetic coils, as listed in Table IV, an electromagnetic manipulation system was developed at the City University of Hong Kong (see Fig. 2). This system consists of six orthogonally aligned identical DT4E-core electromagnetic coils. The effective workspace surrounded by those coils is in a volume of 110 mm diameter. The framework and connection components are made of aluminum, which exerts an insignificant influence on the distribution of the magnetic field. The setup of the entire system, as seen in Fig. 2(b), contains four major functional modules for magnetic field generation, imaging process, magnetic agents, and control.

1) Magnetic Field Generation: Six orthogonally aligned identical DT4E-core electromagnetic coils, indexed by ($i = 1, 2 \dots 6$), are employed to generate a magnetic field. The three upper coils are denoted by even numbers, and the other three are denoted by odd numbers. Each coil is excited by a programmable single-channel dc power supplier, with a maximum output current of 10 A. The resolution of the output current is 0.001 A. Power suppliers are connected to a computer through a RS-232 standard interface. The custom-designed dc power supplier has a maximum current output of 10 A and a minimum response time of 30 ms. The bandwidth of used RS 232 interface is 9600 bps. Two DFK-23G274 CCD cameras with a frame rate of 20 frames/s were employed in the imaging process.

2) Imaging Process: The imaging module consists of two CCD cameras that are located above and below the workspace, two zoomable focus-fixed microscopes, and X-Y-Z motion stages. The camera from the top view provides a 2-D image in the XY plane. The inverted camera below the workspace provides the side view (in Z-axis) of the particle through a 45° prism. The resolution of each CCD camera is 2 megapixels (1600×1200). The X-Y-Z motion stage features a resolution of $0.3215 \mu\text{m}$. The X-Y planar stage is used for monitoring the magnetic agents of interest, and the Z-axis stage is used for installing and focusing the microscope. The obtained image provides position and potentially orientation information of microparticles to the feedback controller.

3) Magnetic Agents: The magnetic agents, which serve as carriers for bringing various biomaterials, must be biocompatible. The functionalized surface of agents, usually based on biomolecules, also senses the status of the surroundings. In our experiments, the used agents were magnetic microparticles, as shown in Fig. 3(a), which were filled with Fe_3O_4 nanoparticles and coated with an inert synthetic polymer, and then, encapsulated in a spherical and hydrophilic agarose polymers. The particles are biocompatible, with a diameter ranging from 5–15 μm and a density of 1.2 g/cm^3 . Fig. 3(b) illustrates the H - M (i.e.,

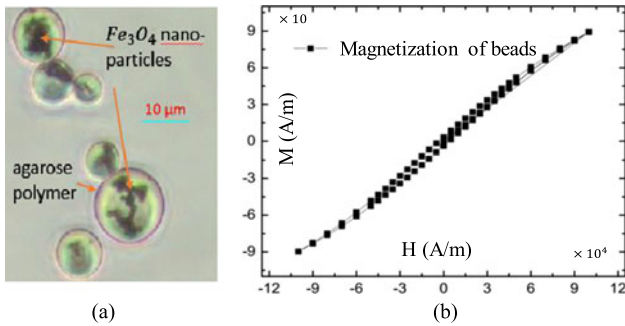


Fig. 3. Magnetic agents. (a) Magnetic microparticles used in experiments. (b) M - H curve of magnetic microparticles measured by SQUID magnetometer.

field strength H and magnetization M) curve, measured by a superconducting quantum interference device (SQUID) magnetometer. Fig. 3(b) illustrates that slight residual magnetization is present in the absence of applied field. Basing on this curve, we could estimate that the susceptibility χ_m is 1.46×10^{-3} (paramagnetic).

4) Control: The control module, which has an Intel core i5 Duo 3.0-GHz processor running Windows 8, is used for providing user commands, such as the desired trajectory, processing the imaging tracking program, and operating the real-time control algorithm. All of these are accomplished through a custom C++ program. The control bandwidth used in this study is 10 Hz. The dc power supply has a minimum response time of 30 ms, which results in a low electromagnetic core-iron loss and relatively less heat accumulation. The current system can work continuously for 1 h before the temperature of coils reaches 50 °C.

Finally, to fabricate an electromagnetic system with the above functional modules, we employed a two-step method for the spatial alignment of coils. The first step is analyzing the chain tolerance, and the second step is calculating the coil orientation. The results of homogeneity of the generated field as well as comparison between the measured and designed data, which are shown in the latter part of this study, have all verified the good alignment accuracy of the fabricated prototype system. The generated magnetic field was calibrated using a linear fitting method based on the error between measured and designed data. A scaling factor could be calculated for each electromagnet by using the least square method, which was then applied to the power supplier to make the magnitude of the generated magnetic field match the designed value.

III. ANALYSIS OF MAGNETIC FIELD DISTRIBUTION FOR ENLARGING WORKSPACE

The spatial distribution of the MFFD B forms a basis not only for designing magnetic manipulation systems but also for supporting closed-loop control. In this section, we present a methodology for the quantitative analysis of magnetic field distribution, which is beneficial to the enlargement of the efficient workspace. The analyzing procedure includes five main steps. The first step is to model the magnetic field by using FEM. The second step is to examine the homogeneity of the generated field for each of the six identical coils. The third step is to ver-

ify that the FEM modeling results match with the experimental results. The fourth step is to demonstrate the linear correlation between the magnetic field distribution and exciting current for a single coil. The fifth step is to establish a magnetic distribution database, based on which the magnetic agents can be manipulated in a larger workspace.

A. Step 1

An FEM analyzing model is developed for simulating the magnetic field generation. The FEM model is performed in ANSYS code (ANSYS, Inc., USA). As shown in Fig. 4(a), each coil is modeled as a thick hollow cylinder with 1720 turns of stranded wire. The cores are made of DT4E material. The other FEM modeling specifications follow the actual parameters of the fabricated system. The maximum current sourced to a coil is 10 A. As shown in Fig. 4(b), we define a global coordinate frame (O -XYZ) for the entire magnetic field and a local coordinate frame ($O - x_1 y_1 z_1$) for Coil_#1. The local coordinate frames for all the coils can be similarly defined as $O - x_k y_k z_k$, where $k = 1 - 6$. All of the origins of these coordinate frames are located at the central point of the workspace, denoted by O .

B. Step 2

To examine homogeneity of the generated field, we used a three-axis Gauss meter to measure the magnitudes of the MFFD along the z_k -axis ($k = 1 - 6$) at six positions, namely $z_k = (5, 15, 25, 35, 45, 55)$ mm, where the exciting current supplied to each coil was 1 A. Fig. 5 illustrates the measured results. The measured results at each position are very similar for all six coils, although the directions of the magnetic field for the six coils differ from one another. Thus, the homogeneity of the six coils can be confirmed. With this confirmation, we can simplify the analysis by studying one single coil only, and the results of all six coils can be calculated by the superposition of all the results of single coils. Coil_#1 is chosen as the example for the study in this paper.

C. Step 3

The FEM model is verified by comparing the modeling results to the experimental data. Fig. 6 illustrates the experimentally measured data and the FEM modeling results of the magnitudes of the MFFD B at the six positions along the centerline of coil_#1, namely $z_1 = 5, 15, 25, 35, 45, 55$ mm, where the exciting current is supplied to coil_#1 (from 1 to 10 A, with a current interval of 1 A). The errors between the experimental measured data and the FEM modeling results are given in Table VI, indicating that the modeling and experimental results exhibit good match. The small difference between the modeling and experimental results are caused by several factors, such as systematic and environmental errors, model uncertainty, current fluctuation, hysteresis-related errors, and magnetic field disturbance.

D. Step 4

According to the Biot-Savart law, the distribution of the MFFD B of each air-core magnetic coil is linearly proportional to the exciting current. Given the use of DT4E-core electromag-

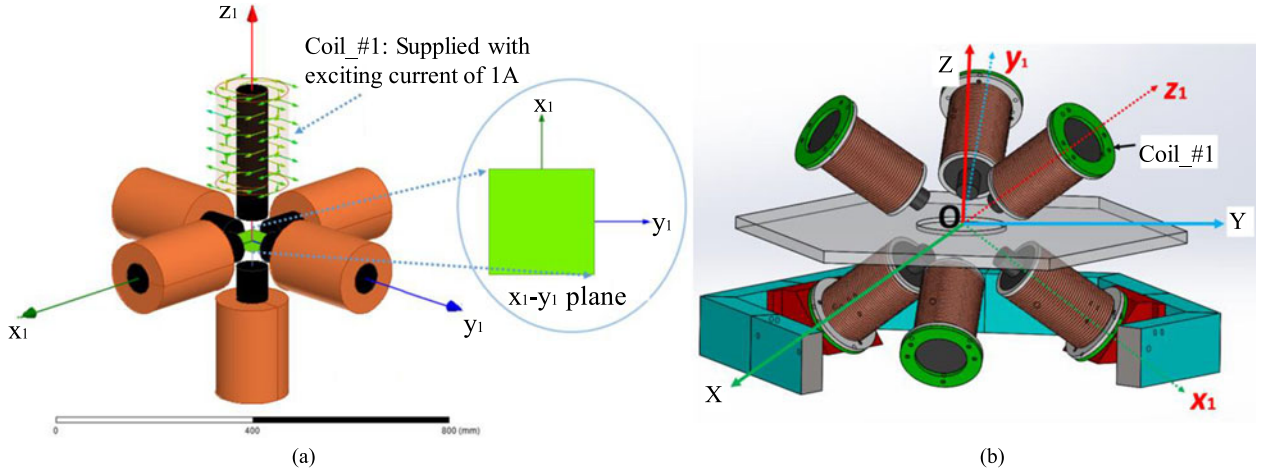


Fig. 4. (a) FEM model of the generated magnetic field. Each electromagnetic coil is labeled with the sequence Coil_# k ($k = 1, 2, \dots, 6$). The first local coordinate frame ($O_1 - xyz$) is shown. The input current of each coil I_k is in anticlockwise direction based on positive z_k -axis. (b) Global coordinate frame ($O - XYZ$) and local coordinate frame ($O - x_1 y_1 z_1$) for Coil_#1.

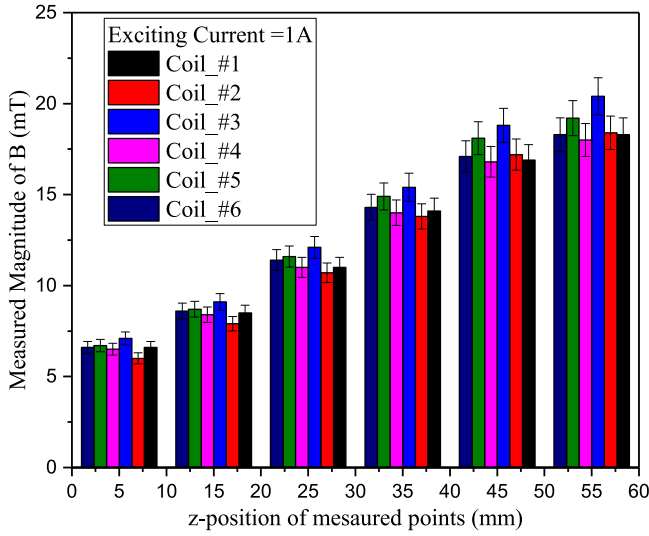


Fig. 5. Demonstration of the homogeneity of the system.

netic coils in our system, we must check whether this linearity relation still holds. As shown in Fig. 6, the magnitude of the MFFD is linearly correlated with the exciting current presumably because the DT4E-cores work in the “linear” part of the B - H curve. These results validate the linear correlation between the magnetic field distribution and the exciting current of each single coil for the developed system.

E. Step 5

Basing on the FEM modeling results, we finally establish a magnetic distribution database. We define a unit vector $\tilde{B}_k(x, y, z)$ as the spatial distribution vector of the MFFD, which is generated by the single coil_# k sourced with an exciting current $I_k = 1$ A. The database consists of \tilde{B}_k of coil_# k in the entire workspace at grid points with distance interval of 0.02 mm. At any (x, y, z) position, $\tilde{B}_k(x, y, z)$ can be calculated by using a linear interpolation method. By defining $B(x, y, z)$ as the magnetic field at the position (x, y, z) , we

TABLE VI
ERRORS BETWEEN EXPERIMENTAL MEASURED DATA AND FEM
ANALYZED RESULTS

Current (A)	55 mm	45 mm	35 mm	25 mm	15 mm	5 mm
1	4.71%	8.05%	6.42%	6.63%	2.05%	6.67%
2	2.66%	3.67%	5.88%	0.13%	4.74%	1.40%
3	0.27%	1.72%	1.67%	3.38%	1.72%	6.97%
4	0.95%	0.56%	0.53%	3.72%	2.31%	5.21%
5	0.57%	1.27%	0.33%	2.55%	1.85%	6.95%
6	2.64%	1.09%	0.68%	5.03%	3.93%	4.63%
7	0.32%	1.25%	1.14%	5.81%	2.22%	6.54%
8	1.12%	2.21%	0.73%	6.39%	1.19%	4.39%
9	5.43%	4.10%	3.32%	6.32%	3.25%	5.66%
10	5.63%	3.93%	3.54%	6.14%	2.42%	7.00%

have

$$B(x, y, z) = \sum_{k=1}^6 B_k(x, y, z). \quad (9)$$

According to the linear correlation between the magnetic field distribution and the exciting current for a single coil, we have

$$B_k = \tilde{B}_k I_k. \quad (10)$$

By substituting (10) into (9), the magnetic field can be written as follows:

$$B(x, y, z) = \sum_{k=1}^6 \tilde{B}_k I_k. \quad (11)$$

Based on the above models, a unit electromagnetic field distribution database for a 3-D grid of points is established, and the generated magnetic field at these specified points under the current input $I = [I_1, I_2, I_3, I_4, I_5, I_6]^T$ can be calculated. In the other points of the workspace, trilinear interpolation can be used to calculate the generated field. With the magnetic field information, the microparticle can be manipulated affectively in a larger workspace than the central area only.

Note that the above modeling approach is numerical analysis based. Several works on the analytical model development,

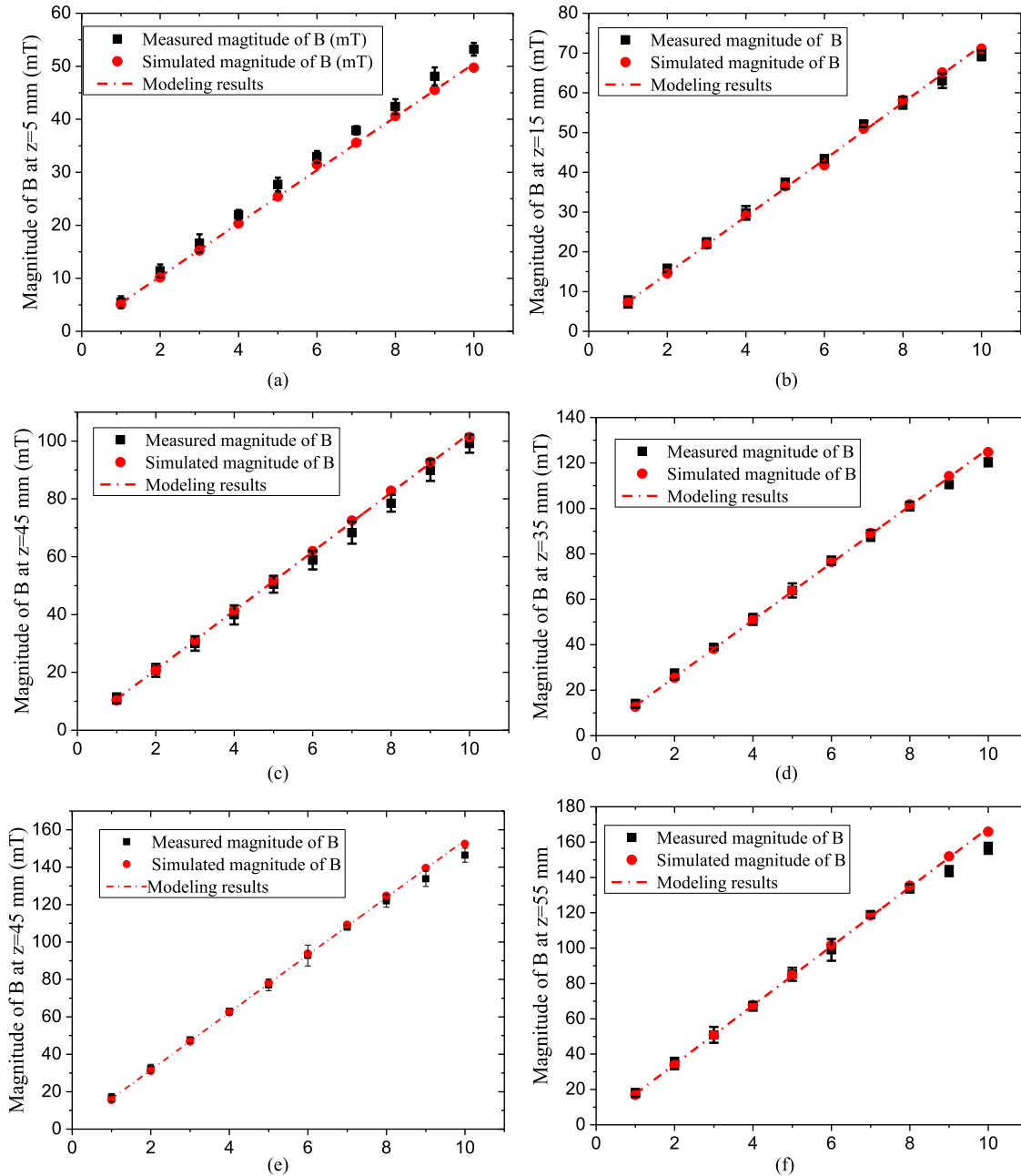


Fig. 6. Experimental and FEM modeling results of the magnitude of B at six positions along the centerline of coil_#1, namely $z_1 = 5, 15, 25, 35, 45, 55$ mm, where dash-dot lines denote the linear fitting results based on the modeling data, cubes denote the measured magnitude of B , and circles denote the simulated magnitude of B .

which mainly focused on manipulation of microparticles in the central area of the workspace, such as [8], [20], [28], have been reported in the literature.

The developed database can serve to calculate many important variables of the magnetic field through numerical study. Fig. 7(a) illustrates the magnetic field distribution in a planar area of 110×110 mm² for coil_#1, where both the magnitude and the orientation of the vectors are shown. The magnitude of the MFFD is approximately 4.44 mT when coil_#1 is supplied with an exciting current of 1 A. A good match between results in Figs. 5 and 6 is noted. As the capacity of the maximum current output is 10 A, the MFFD can reach approximately 40 mT when

a single coil is sourced. When the other coils are considered, the MFFD can reach a magnitude of 100 mT in total. Fig. 7(b) shows the details of the vector orientation of the MFFD. In the region of the central area of 20 mm diameter, B vectors are nearly in parallel and the magnitude of ∇B is nearly the same. This explains why the magnetic agents are ideally manipulated in the central region, with a nearly uniform gradient. Fig. 8 shows the magnitude of the magnetic field gradient, where the maximum value is approximately 0.29 T/m when the coil is supplied with a 1-A exciting current. As the maximum current capacity is 10 A, the gradient of MFFD can reach approximately 2.5 T/m.

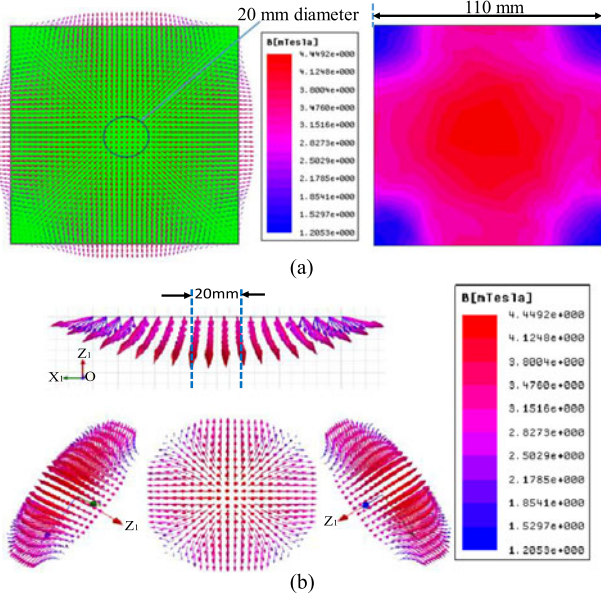


Fig. 7. Analysis of magnetic field distribution. (a) Distribution of magnitude and vector orientation of the MFFD in the $x-y$ plane of $O - x_1y_1z_1$, when coil_#1 is applied with an exciting current of 1 A. (b) MFFD vectors distributed in the $x-y$ plane of $O - x_1y_1z_1$.

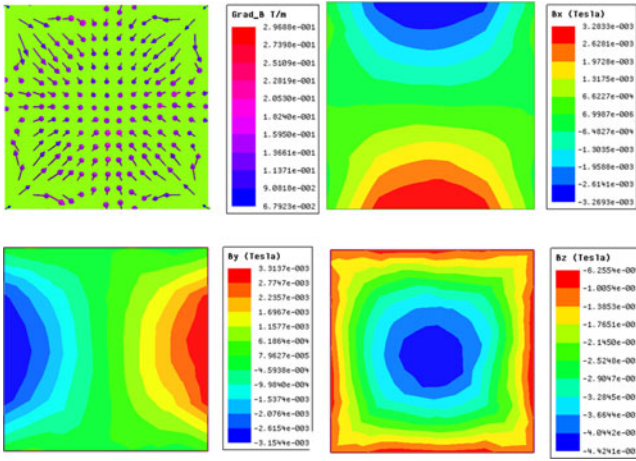


Fig. 8. Distribution of ∇B and $|B_x|$, $|B_y|$, $|B_z|$.

IV. EXPERIMENTAL DETAILS

Experiments were performed to demonstrate the developed system and the actuation strategy. The microparticles used in experiments featured a diameter of $10 \mu\text{m}$ and a density of $1.2 \times 10^3 \text{ kg/m}^3$. To overcome the effects caused by gravity and friction, the medium used was light-salted water, and its density was adjusted to be similar to that of the particle. The particles were syringed on a slide placed in the XY plane of the workspace, as shown in Fig. 9(a). A visual-based proportional and integral controller was employed for the automated motion control of the microparticles. The image of the microparticle was captured through image processing, and the geometrical center of each particle was used to define the particle's position.

We initially demonstrated that the microparticles can be manipulated in a large workspace. Five different regions, namely the central region around the workspace center and the first to

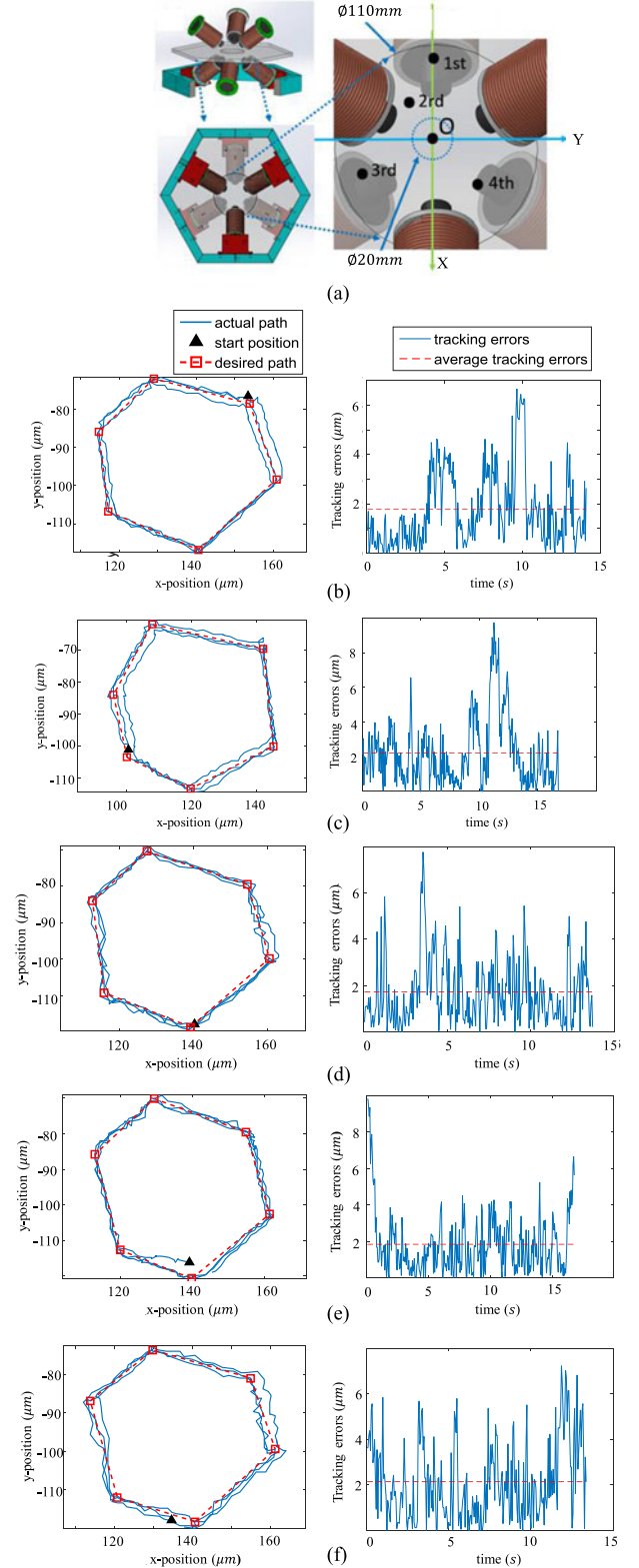


Fig. 9. Experimental results of tracking control. (a) Selected regions for experiments. Centers of each region are central region ($X = 0 \text{ mm}$, $Y = 0 \text{ mm}$), first region ($X = 0 \text{ mm}$, $Y = 42.1 \text{ mm}$), second region ($X = -11.3 \text{ mm}$, $Y = 16.8 \text{ mm}$), third region ($X = -36.1 \text{ mm}$, $Y = -15.7 \text{ mm}$), and fourth region ($X = 22.3 \text{ mm}$, $Y = -21.9 \text{ mm}$). (b) Tracking results in the central region. (c) Tracking results in the first region. (d) Tracking results in the second region. (e) Tracking results in the third region. (f) Tracking results in the fourth region. The left figures are trajectories in the XY plane. The right figures show the errors between actual and desired trajectories. All motions are in the clockwise direction.

TABLE VII
EXPERIMENTAL RESULTS

Parameters	Center Position	First Position	Second Position	Third Position	Fourth Position
Average completion time (s)	14.15	16.75	13.70	16.80	13.35
Average tracking speed ($\mu\text{m/s}$)	31.99	31.67	36.54	29.81	36.01
Average tracking error (μm)	1.77	2.22	1.74	1.83	2.15
Maximum tracking error (μm)	6.65	9.74	7.76	9.80	7.22

fourth regions, which are all far away from the central area, were selected for performing experiments. As seen in Fig. 9(a), the centers of the five regions are ($X = 0 \text{ mm}$, $Y = 0 \text{ mm}$) for the central region, and ($X = 0 \text{ mm}$, $Y = 42.1 \text{ mm}$), ($X = -11.3 \text{ mm}$, $Y = 16.8 \text{ mm}$), ($X = -36.1 \text{ mm}$, $Y = -15.7 \text{ mm}$), ($X = 22.3 \text{ mm}$, $Y = -21.9 \text{ mm}$) for the first to fourth regions. The first region was chosen to be 42 mm away from the center of the workspace, which is near the edge of the workspace. In each region, the moving trajectory was predesigned, based on which time-vary currents were calculated according to the field distribution database. The currents were then input to the electromagnetic coils. During the experiments, the maximum current was 7.8 A. All the tracking tests at each position were repeated for three times. Fig. 9(b)–(f) illustrates the experimental results of the trajectory path and the tracking errors (i.e., measured by Euclidean distance) of the controlled particle in each region. During the manipulations, the multi-DOF motion was fully decoupled. These results clearly indicate that the tracking performance of the particles in all the regions is as good as that in the central area. Table VII summarizes the experimental results, which demonstrate the capacity of the developed system for precise tracking control of microparticles in a relatively large workspace. Given that the controlled motion of the particles was based on the analysis of the magnetic field distribution, these results also validate the accuracy of the established database.

We further performed experiments of moving a microparticle along a 3-D helix-like curve to test the manipulation capacity of the developed system in a 3-D scenario. Some of the testing results were also reported in [31]. Tracking process at different time instants, viewed from both the top and the side of the workspace, is shown in Fig. 10(a)–(c). Fig. 10(d) illustrates the 3-D path in the trajectory tracking. Fig. 10(e) illustrates the motion trajectory of the controlled particle from the top and side views, respectively. The mean-squared errors of trajectory tracking were $5.06 \mu\text{m}$ in X -axis, $6.28 \mu\text{m}$ in Y -axis, and $3.51 \mu\text{m}$ in Z -axis. The completion time was 33 s. These results well demonstrate the effectiveness of the developed electromagnetic system in achieving 3-D trajectory tracking of microparticles.

V. CONCLUSION

This paper presents the development of a new electromagnetic actuation system for noncontact untethered manipulation

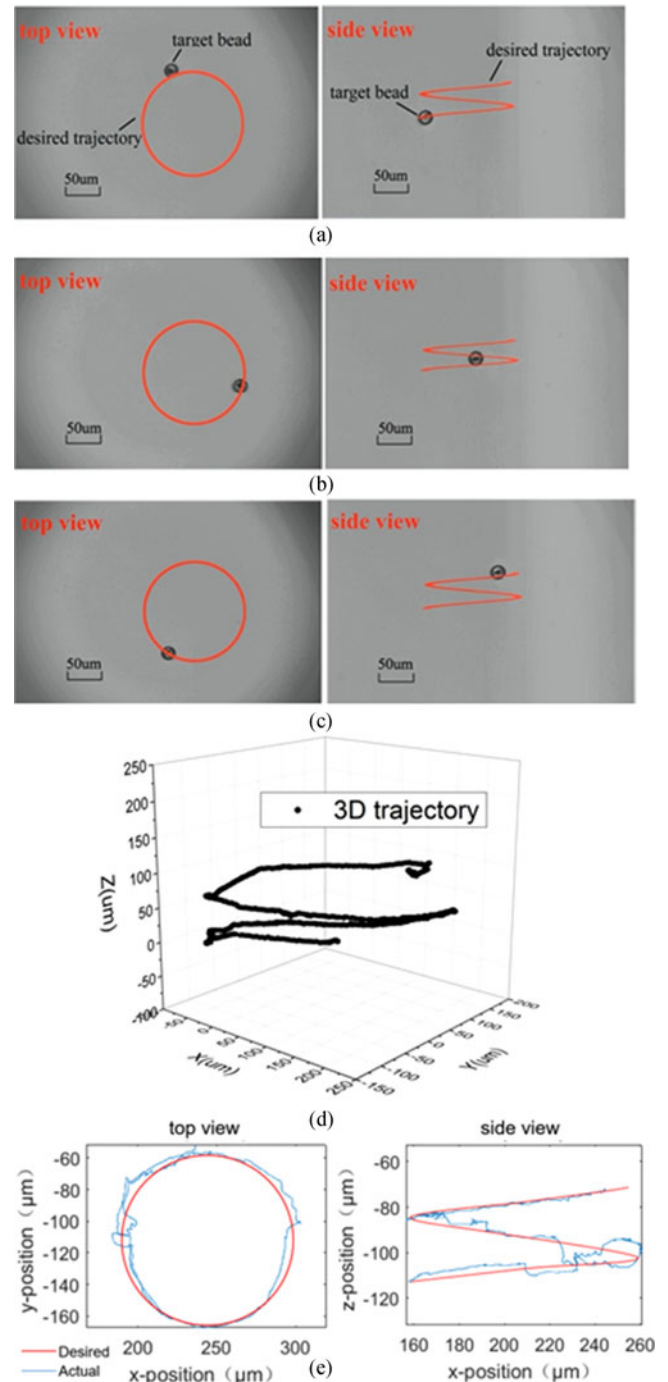


Fig. 10. Experimental results of tracking a microparticle along a 3-D helix-like curve. (a) $t = 0 \text{ s}$. (b) $t = 16 \text{ s}$. (c) $t = 33 \text{ s}$. (d) Three-dimensional trajectory path. (e) Motion trajectory of the controlled particle from the top and side views.

of magnetic microparticles. The developed system and the actuation strategy can facilitate the precise manipulation of microparticles in a large workspace, which are surrounded by six orthogonally aligned identical electromagnetic coils. The effective workspace can be enlarged mainly by the two reasons. First, we have characterized the influence of electromagnet parameters, such as position, radius, and height of cores, on the generated electromagnetic field, and then, designed an electro-

magnetic coils system that can reach a spherical volume with 110 mm diameter, a MFFD of 100 mT, and a magnetic field gradient of 2.5 T/m. Both the size of the workspace and the strength of the generated magnetic field are adequate for conducting many manipulation tasks. Second, we have modeled and analyzed the spatial distribution of the electromagnetic field quantitatively, and then, established an electromagnetic field distribution database. Compared to most existing designs, where the motions of microparticles are restricted at the central area of the workspace, the developed system can manipulate the microparticles effectively at a much larger workspace rather than the central area only. Availability of the field distribution database benefits not only the machine design but also the manipulation of the microparticles controlled by the machine. To demonstrate the effectiveness of the designed integrated machine, we have performed experiments for an effective tracking control of the microparticles in both 2-D and 3-D scenarios.

Our future study will include the investigation of singularity problem under the six-coil electromagnetic system, development of an analytical model of the coil system for working in a large workspace, and improvement of the current system in several aspects, such as increasing control bandwidth and adding a cooling system. We also plan to extend the current study to more complex environments, such as *in vivo* biomedical scenarios. To meet the need of *in vivo* clinical applications, more effective tracking and control methods supported by a high-rate imaging feedback will be investigated.

REFERENCE

- [1] M. Sitti *et al.*, "Biomedical applications of untethered mobile milli/microrobots," *Proc. IEEE*, vol. 103, no. 2, pp. 205–224, Feb. 2015.
- [2] F. Tendick, S. S. Sastry, R. S. Fearing, and M. Cohn, "Applications of micromechatronics in minimally invasive surgery," *IEEE/ASME Trans. Mechatronics*, vol. 3, no. 1, pp. 34–42, Mar. 1998.
- [3] B. J. Nelson, I. K. Kaliakatos, and J. J. Abbott, "Microrobots for minimally invasive medicine," *Annu. Rev. Biomed. Eng.*, vol. 12, pp. 55–85, 2010.
- [4] A. M. Flynn, K. Udayakumar, D. S. Barrett, J. D. McLurkin, D. L. Franck, and A. Shectman, "Tomorrow's surgery: Micromotors and microrobots for minimally invasive procedures," *Minimally Invasive Ther.*, vol. 7, no. 4, pp. 343–352, 1998.
- [5] M. Sitti and H. Hashimoto, "Controlled pushing of nanoparticles: Modeling and experiments," *IEEE/ASME Trans. Mechatronics*, vol. 5, no. 2, pp. 199–211, Jun. 2000.
- [6] J. J. Abbott, M. C. Lagomarsino, L. Zhang, L. Dong, and B. J. Nelson, "How should microrobots swim?" *Int. J. Robot. Res.*, vol. 66, pp. 157–167, 2009.
- [7] H. Ishihara, F. Arai, and T. Fukuda, "Micro mechatronics and micro actuators," *IEEE/ASME Trans. Mechatronics*, vol. 1, no. 1, pp. 68–79, Mar. 1996.
- [8] J. Abbott, Z. Nagy, F. Beyeler, and B. Nelson, "Robotics in the small, Part I: Microbotics," *IEEE Robot. Autom. Mag.*, vol. 14, no. 2, pp. 92–103, Jun. 2007.
- [9] J. F. Schenck, "Safety of strong, static magnetic fields," *J. Magn. Reson. Imag.*, vol. 12, no. 1, pp. 2–19, 2000.
- [10] Q. A. Pankhurst, J. Connolly, S. Jones, and J. Dobson, "Applications of magnetic nanoparticles in biomedicine," *J. Phys. D, Appl. Phys.*, vol. 36, no. 13, pp. 167–181, 2003.
- [11] S. H. Kim and K. Ishiyama, "Magnetic robot and manipulation for active-locomotion with targeted drug release," *IEEE/ASME Trans. Mechatronics*, vol. 19, no. 5, pp. 1651–1659, Oct. 2014.
- [12] S. Yim, K. Goyal, and M. Sitti, "Magnetically actuated soft capsule with the multimodal drug release function," *IEEE/ASME Trans. Mechatronics*, vol. 18, no. 4, pp. 1413–1418, Aug. 2013.
- [13] K. B. Yesin, K. Vollmers, and B. J. Nelson, "Modeling and control of untethered biomicrobots in a fluidic environment using electromagnetic fields," *Int. J. Robot. Res.*, vol. 25, nos. 5/6, pp. 527–536, 2006.
- [14] A. J. Petruska, A. W. Mahoney, and J. J. Abbott, "Remote manipulation with a stationary computer-controlled magnetic dipole source," *IEEE Trans. Robot.*, vol. 30, no. 5, pp. 1222–1227, Oct. 2014.
- [15] G. Go *et al.*, "Electromagnetic navigation system using simple coil structure (4 coils) for 3-D locomotive microrobot," *IEEE Trans. Magn.*, vol. 51, no. 4, Apr. 2015, Art. no. 8002107.
- [16] S. Jeong, H. Choi, J. Choi, C. Yu, J.-O. Park, and S. Park, "Novel electromagnetic actuation (EMA) method for 3-dimensional locomotion of intravascular microrobot," *Sens. Actuators A, Phys.*, vol. 157, no. 1, pp. 118–125, 2010.
- [17] M. P. Kummer, J. J. Abbott, B. E. Kratochvil, R. Borer, A. Sengul, and B. J. Nelson, "OctoMag: An electromagnetic system for 5-DOF wireless micromanipulation," *IEEE Trans. Robot.*, vol. 26, no. 6, pp. 1006–1017, Dec. 2010.
- [18] F. Niu, W. Ma, H. K. Chu, H. Ji, J. Yang, and D. Sun, "An electromagnetic system for magnetic microbead's manipulation," in *Proc. IEEE Int. Conf. Mechatron. Autom.*, 2015, pp. 1005–1010.
- [19] A. W. Mahoney and J. J. Abbott, "Generating rotating magnetic fields with a single permanent magnet for propulsion of untethered magnetic devices in a lumen," *IEEE Trans. Robot.*, vol. 30, no. 2, pp. 411–420, Apr. 2014.
- [20] C. Pawashe, S. Floyd, and M. Sitti, "Modeling and experimental characterization of an untethered magnetic micro-robot," *Int. J. Robot. Res.*, vol. 28, no. 8, pp. 1077–1094, 2009.
- [21] S. Tottori, L. Zhang, F. Qiu, K. K. Krawczyk, A. Franco-Obrégón, and B. J. Nelson, "Magnetic helical micromachines: Fabrication, controlled swimming, and cargo transport," *Adv. Mater.*, vol. 24, no. 6, pp. 811–816, 2012.
- [22] A. Servant, F. Qiu, M. Mazza, K. Kostarelos, and B. J. Nelson, "Controlled *in vivo* swimming of a swarm of bacteria-like microrobotic flagella," *Adv. Mater.*, vol. 27, no. 19, pp. 2981–2988, 2015.
- [23] S. Martel, M. Mohammadi, O. Felfoul, Z. Lu, and P. Pouponneau, "Flagellated magnetotactic bacteria as controlled MRI-trackable propulsion and steering systems for medical nanorobots operating in the human microvasculature," *Int. J. Robot. Res.*, vol. 28, no. 4, pp. 571–582, 2009.
- [24] S. H. Kim, K. Shin, S. Hashi, and K. Ishiyama, "Magnetic fish-robot based on multi-motion control of a flexible magnetic actuator," *Bioinspiration Biomimetics*, vol. 7, no. 3, pp. 036007(13pp), 2012.
- [25] S. Yim and M. Sitti, "Design and rolling locomotion of a magnetically actuated soft capsule endoscope," *IEEE Trans. Robot.*, vol. 28, no. 1, pp. 183–194, Feb. 2012.
- [26] Z. Zhang, Y. Huang, and C.-H. Menq, "Actively controlled manipulation of a magnetic microbead using quadrupole magnetic tweezers," *IEEE Trans. Robot.*, vol. 26, no. 3, pp. 531–541, Jun. 2010.
- [27] S. Floyd, C. Pawashe, and M. Sitti, "An untethered magnetically actuated micro-robot capable of motion on arbitrary surfaces," in *Proc. IEEE Int. Conf. Robot. Autom.*, 2008, pp. 419–424.
- [28] E. Diller, J. Giltinan, G. Z. Lum, Z. Ye, and M. Sitti, "Six-degree-of-freedom magnetic actuation for wireless microrobotics," *Int. J. Robot. Res.*, vol. 35, nos. 1–3, pp. 114–128, 2015.
- [29] I. S. Khalil, J. D. Keuning, L. Abelmann, and S. Misra, "Wireless magnetic-based control of paramagnetic microparticles," in *Proc. IEEE Int. Conf. Biomed. Robot. Biomechatron.*, 2012, pp. 460–466.
- [30] J. J. Abbott, O. Ergeneman, M. P. Kummer, A. M. Hirt, and B. J. Nelson, "Modeling magnetic torque and force for controlled manipulation of soft-magnetic bodies," *IEEE Trans. Robot.*, vol. 23, no. 6, pp. 1247–1252, Dec. 2007.
- [31] W. Ma, J. Li, F. Niu, H. Ji, and D. Sun, "Robust control to manipulate a microparticle with electromagnetic coil system," *IEEE Trans. Ind. Electron.*, vol. 64, 2017. doi: [10.1109/TIE.2017.2701759](https://doi.org/10.1109/TIE.2017.2701759)



Fuzhou Niu received the B.S. degree from the Department of Precision Machinery and Instrumentation, University of Science and Technology of China, Hefei, China, in 2010. He is currently working toward the Ph.D. degree jointly with the University of Science and Technology of China, and the City University of Hong Kong, Kowloon, Hong Kong.

His research interests include electromagnetic system design and applications.



Junyang Li received the B.S. and M.S. degrees from the Department of Measurement Technology and Instrument, North University of China, Taiyuan, China, in 2011 and 2014, respectively. He is currently working toward the Ph.D. degree with the City University of Hong Kong, Kowloon, Hong Kong.

His research interests include design and fabrication of magnetic microrobots by 3-D laser lithography for tissue regeneration and drug delivery.



Weicheng Ma received the B.S. degree from the Department of Automation, University of Science and Technology of China, Hefei, China, in 2011, and the Ph.D. degree jointly from the University of Science and Technology of China and the City University of Hong Kong, Kowloon, Hong Kong, in 2017.

Her research interests include electro-magnetic-based manipulation and nonlinear control applications.



Jie Yang received the B.S. degree from the Department of Physical Chemistry, Beijing University of Science and Technology, Beijing, China, in 1969.

He is currently a Professor with the Department of Precision Machinery and Precision Instrumentation, University of Science and Technology of China, Hefei, China. He has led a research group focusing on robotics supported by the National Science Foundation of China and the 863 Projects. His research interests

include intelligent robots, shape memory materials, and high-speed photography.



Dong Sun (F'15) received the bachelor's and master's degrees from the Mechanical and Biomedical Engineering Department, Tsinghua University, Beijing, China, in 1990 and 1994, respectively, and the Ph.D. degree in robotics and automation from the Chinese University of Hong Kong, Shatin, Hong Kong, in 1997.

After performing his postdoctoral research at the University of Toronto, Toronto, ON, Canada, he joined the City University of Hong Kong, Kowloon, Hong Kong, as an Assistant Professor,

in 2000. He is currently a Chair Professor and Head of the Department of Mechanical and Biomedical Engineering, City University of Hong Kong. His main research interests include robotics and the related biomedical engineering, particularly for cellular engineering applications.

Dr. Sun has served on editorial boards for several prestigious international journals, such as the IEEE TRANSACTIONS ON ROBOTICS and the IEEE/ASME TRANSACTIONS ON MECHATRONICS. He received numerous Best Paper Awards from international journal and conferences, as well as industrial awards, such as the Hong Kong Awards for Industry. He has organized several international conferences as the General or Program Chair.